RESEARCH ARTICLE | SEPTEMBER 23 2025

Mitigating the film–substrate decohesion in nanoporous metals

Gideon Henkelmann ; Xinyan Wu ; Jörg Weissmüller

APL Mater. 13, 091116 (2025)
https://doi.org/10.1063/5.0287477

Mitigating the film–substrate decohesion in nanoporous metals

Cite as: APL Mater. 13, 091116 (2025); doi: 10.1063/5.0287477
Submitted: 25 June 2025 • Accepted: 3 September 2025 •
Published Online: 23 September 2025

Gideon Henkelmann,[1] Xinyan Wu,[2] and Jörg Weissmüller[1,3,a)]

AFFILIATIONS

[1] Institute of Materials Physics and Technology, Hamburg University of Technology, Hamburg, Germany
[2] Institute of Optical and Electronic Materials, Hamburg University of Technology, Hamburg, Germany
[3] Institute of Hydrogen Technology, Helmholtz-Zentrum Hereon, Geesthacht, Germany

[a)] **Author to whom correspondence should be addressed:** weissmueller@tuhh.de

ABSTRACT

Substrate-supported films of dealloyed nanoporous metals spontaneously develop a low-connectivity layer at the film–substrate interface, impairing interfacial adhesion strength. Comparable interfacial degradation has been reported for sintered interconnects in microelectronics. The phenomenon arises from a divergence in the diffusive, curvature-driven flux of the material, normal to the interface. This reduces the local solute fraction and eventually leads to disconnection by a Plateau–Rayleigh-type instability. Comparing dealloying and subsequent coarsening in experiments and kinetic Monte Carlo simulation, this work investigates mitigation strategies and, in particular, the effect of distinct porosity–depth profiles on the interfacial connectivity. Two design principles are suggested: First, the profile should be smooth, avoiding jumps and kinks. Second, steep porosity gradients should be placed in low-porosity regions. Exponential profiles are found preferable for avoiding degradation. In the fields of nanoporous thin films as functional materials and of interconnects in microelectronics joining, the findings provide the basis for materials design toward enhanced adhesion and lifetime.

I. INTRODUCTION

Thin films of dealloyed nanoporous metals, particularly nanoporous gold, are promising functional materials with a broad range of applications, including substrates for surface-enhanced Raman scattering,[1,2] controlled drug release,[3] photocatalysis,[4] filtration,[5] supercapacitor electrodes,[6–8] cantilever-based actuation and sensing,[9–13] energy conversion systems,[7] and microelectronic interconnects.[14,15] In all these systems, the porous film is typically bonded to a massive (not porous) substrate, and the adhesion strength at the film–substrate interface is a key factor for device performance. A recurring issue in such systems is the spontaneous loss of connectivity between dealloyed nanoporous films and their substrates; see references and discussion in Ref. 16. The elimination of contact area between the film and substrate resembles the dewetting of solid films,[17–19] yet its driving force is quite different. While the tendency for dewetting is controlled by the substrate–film hetero-interface energy, porous film decohesion is prompted by gradients in the laterally averaged mean curvature of the pore surfaces in a material of uniform composition.

The connectivity loss has been traced to discontinuities in the depth profile (along the film normal) of the laterally averaged mean curvature. These discontinuities cause divergence of curvature-driven surface mass transport normal to the substrate, ultimately leading to increased porosity and to local disconnection, near the interface, by a Plateau–Rayleigh-type instability.[16] Since such curvature discontinuities are intrinsic to porous–film–on–substrate configurations, the resulting interfacial degradation may pose a general challenge for porous thin-film systems. Indeed, a similar behavior has also been reported in microelectronics joining, particularly in pressureless sintered silver-paste interconnects, where comparable interfacial weakening is observed (see Figs. 6 and 8 in Ref. 20).

Here, we address the above issues by combining experiments on nanoporous gold thin films made by dealloying silver–gold solid solutions with atomistic kinetic Monte Carlo (KMC) simulations. We study the microstructure evolution to identify design strategies that improve long-term adhesion at the interface of the porous film with its substrate.

Our working hypothesis is based on the physical mechanism underlying detachment: gradients or abrupt changes in the

microstructure lead to diffusion flux divergence and ultimately to a loss of connectivity. This suggests that smooth, continuous transitions in porosity may mitigate interfacial detachment. In addition, previous studies indicate that structures with higher solid fractions are less prone to disconnection than those with more dilute ones.[21] Thus, placing the film–substrate interface within a region of high solid fraction may enhance adhesion. However, many functional applications rely on open, low-density porous structures to ensure high surface area or permeability. To reconcile these competing requirements, we investigate films with a bulk region of uniform low-density and with a transition layer, near the interface with the substrate, exhibiting a gradient in solid fraction.

To realize the porosity gradients, we exploit the fact that dealloying transfers the composition profile of the master alloy into a porosity profile in the resulting film. Tailoring the local composition of the master alloy thus affords control over the porosity profile along the film depth.

A natural approach to a composition gradient at the interface between a gold substrate and an initially uniform silver–gold film is annealing for smoothing out the composition step by interdiffusion. Yet, rapid diffusion along grain boundaries between the film's columnar grains is well documented[22–25] and will likely result in laterally heterogeneous composition profiles. Therefore, our experimental approach to master alloy films with graded composition is based on controlling the deposition rates of the constituents during sputter deposition of the Au–Ag film.

In experiment, different preparation strategies may favor different profiles in master-alloy composition or porosity. Our KMC simulations systematically assess several types of profiles, specifically linear, staircase-like, and exponential gradients. Experimental validation using matched composition profiles confirms the simulation results.

II. METHODS

Substrate-supported nanoporous gold (NPG) thin films were fabricated following procedures detailed in Ref. 16. In brief, the deposition was performed via DC magnetron sputtering in a chamber with 5×10^{-7} mbar base pressure, using 100 μm-thick (100)-oriented silicon wafers as substrates. These were cleaned by *in situ* Ar plasma etching. A Ti adhesion layer (6–8 nm) was deposited first, followed by ~50 nm of pure Au and subsequently about 550 nm of the AuAg precursor alloy. Uniform composition films were made by sputtering from an $Au_{25}Ag_{75}$ alloy target. Gradient samples were produced by co-sputtering from the $Au_{25}Ag_{75}$ alloy and pure Au targets, using a constant power on the alloy target while gradually reducing the Au target power to generate the desired composition gradient. Each deposition concluded with sputtering from the alloy target only.

The primary dealloying method was electrochemical dealloying in 1M $HClO_4$. The thin film, acting as the working electrode, was mounted in a custom-made Teflon holder. A pseudo-Ag/AgCl reference electrode (0.51 V vs reversible hydrogen electrode (RHE) in 1M $HClO_4$) was used, and a coiled silver wire served as the counter electrode. Dealloying was conducted at 1.26 V vs RHE for up to 30 min. Additional samples, presented in the supplementary material, were dealloyed by free corrosion in 65% HNO_3 at room temperature, for up to 60 min.

Cross sections for scanning electron microscopy (Zeiss Supra 55 VP operated at 10 kV in in-lens mode) were prepared by focused Ar-ion beam milling (Leica TIC 3X). For screening different composition profiles and dealloying durations, some cross sections were alternatively imaged directly after mechanical cleavage. Here, gently indenting an edge of the substrate wafer with a diamond scriber promoted cleavage of the wafer–film assembly, typically along a (010) plane of the wafer. Thin lamellae (~100 nm thick) for transmission electron microscopy (TEM) were prepared using a focused Ga-ion beam (FEI Helios G3 UC) and analyzed using an FEI Talos F200X TEM operated at 200 kV, equipped with an energy-dispersive x-ray spectroscopy (EDS) system.

On-lattice KMC simulations followed previously established protocols.[16] The cuboidal simulation domain consisted of face-centered cubic unit cells with a free (111)-oriented top surface and periodic boundary conditions in the lateral directions. A pure Au bottom layer (7.5 nm thick) represented the substrate; the top 7.5 nm was left empty. The intermediate region, ~60 nm by 60 nm in cross section and 75 nm thick and containing ~16×10^6 sites, was randomly populated with Ag and Au atoms. The in-plane mean Au atom fraction, x_{Au}, was set according to the desired composition profile. In each case, the gradient transitioned into a bulk region extending to the free surface with $x_{Au} = 0.25$.

For clarity, we define x_{Au} here as the lateral average of lattice site occupancy by Au atoms. Non-Au sites are either occupied by Ag or vacant. In the absence of Ag, x_{Au} corresponds to the solid volume fraction, that is, one minus the porosity.

Following standard methodologies,[16,21,26–30] the set of allowed events was restricted to Ag dissolution and diffusion of both Ag and Au. Only atoms with nine or fewer neighbor atoms were eligible for these events, and diffusion targets were restricted to vacant sites with at least three neighbor atoms (including the diffusing one). Event rates for diffusion, k_{dif}, and dissolution, k_{dis}, followed the bond-breaking model,[26]

$$k_{dif} = \nu_{dif} \exp\left(-\frac{nE_b}{k_B T}\right), \tag{1}$$

$$k_{dis} = \nu_{dis} \exp\left(-\frac{nE_b - e\phi}{k_B T}\right). \tag{2}$$

Here, ν_{dif} and ν_{dis} represent diffusion and dissolution attempt frequencies, respectively, n is the number of neighboring atoms, E_b is the bond energy, k_B is Boltzmann's constant, T is the absolute temperature, e is the elementary charge, and ϕ is the electrode potential. Parameter values were adopted from Ref. 26, in particular, $\nu_{dif} = 10^{13}$ s^{-1}, $\nu_{dis} = 10^4$ s^{-1}, and $E_b = 0.15$ eV. Simulations were performed at $T = 300$ K and $\phi = 1.1$ V. We visualized configurations using the TACHYON ray tracer integrated in the OVITO software.[31]

Simulation time advanced incrementally by $\Delta t = -\ln(c)/\sum_i k_i$, where c is a random number in [0, 1] and $\sum_i k_i$ is the total rate of all possible events.[32] Note that simulation time scales are not quantitatively matched to experiment, as the event rates are based on standard values. Accordingly, the simulations capture qualitative aspects of time evolution rather than quantitative kinetics.

III. RESULTS

Our KMC simulations of dealloying and coarsening examined four types of precursor composition profiles: uniform, staircase, linear, and exponential. The supplementary material includes time-lapse videos in logarithmic time scale of all simulation results.

Consistent with earlier studies, the simulations reproduced the characteristic two-stage evolution of nanoporous structure formation. In the primary dealloying phase, the corrosion front advanced from the surface toward the substrate, forming an initial, very fine-scaled network of pores. This process typically lasted ~20 min, with duration varying slightly depending on the composition profile. In the subsequent secondary dealloying phase, the structure coarsened via surface diffusion, while residual Ag was gradually removed. The simulation followed this process for ~10 d.

As a benchmark, we studied dealloying of a uniform $Au_{25}Ag_{75}$ master alloy film. Figure 1 compiles the results. The cross-sectional electron micrograph in panel (a) shows the film after extensive secondary dealloying. The pronounced detachment from the substrate is obvious, with the low-connectivity layer at the film–substrate interface showing as a distinct dark gap. KMC simulations in panels (b) and (c) reproduce this behavior: although the porous film remains connected immediately after primary dealloying, secondary dealloying leads to a significant Au depletion and severe connectivity loss at the film–substrate interface. These results confirm earlier findings reported in Ref. 16.

Next, we investigated a staircase composition profile, where the master alloy Au fraction decreases from $x_{Au} = 0.50$ at the substrate to $x_{Au} = 0.25$ at the border with the uniform layer, across five discrete steps. The composition near the substrate interface lies just above the parting limit of $x_{Au} = 0.45$, preventing the corrosion front from reaching the substrate.[30]

Simulation snapshots in Fig. 2 illustrate how the dealloying progresses only slowly into the denser regions of the master alloy, leading to a gradual decrease in porosity with depth. As in the uniform profile, primary dealloying leaves the solid phase well connected, while coarsening during secondary dealloying induces localized density loss. The corresponding density profiles reveal low-density regions (downward peaks in the fraction of occupied sites) forming at each composition step in the initial master alloy. The most pronounced minimum occurs at the topmost step, leading to almost complete detachment. This step corresponds to the interface with the master alloy region of lowest x_{Au}. That region also exhibits the lowest solid fraction after dealloying, consistent with the known trend that Au-dilute master alloys yield higher porosity. This is natural, as the crystal lattice is preserved and dealloying replaces Ag atoms with vacancies, which subsequently coalesce to form pore space.

Evidently, the connectivity loss is most severe where the initial porosity is highest. This observation aligns with the established trend that lower initial solid fractions entail increased susceptibility to connectivity loss.[21]

Next, Fig. 3 shows the results of a linear composition gradient, where x_{Au} decreases continuously from 0.50 at the substrate interface to 0.25 at the transition to the uniform $Au_{25}Ag_{75}$ region. Panel (a) shows an EDS map confirming the gradient. Panel (b) presents electron micrographs recorded on samples dealloyed for different periods. In the sample dealloyed for the shortest period (1 min), the porous film appears well connected. By contrast, regions of low connectivity are seen to have developed in the sample dealloyed for 10 min. These regions have extended and merged to an almost contiguous low-density layer in the sample dealloyed for 30 min. The location, in depth, of that low-density layer agrees quite precisely with the kink in the composition profile at the transition between the gradient and uniform composition [see panel (a)]. Wider field-of-view micrographs of the same samples are presented in Fig. S4 of the supplementary material. KMC simulation results shown in panels (c) and (d) confirm this finding: reduced solid fraction and connectivity loss appear at the position of the initial composition kink

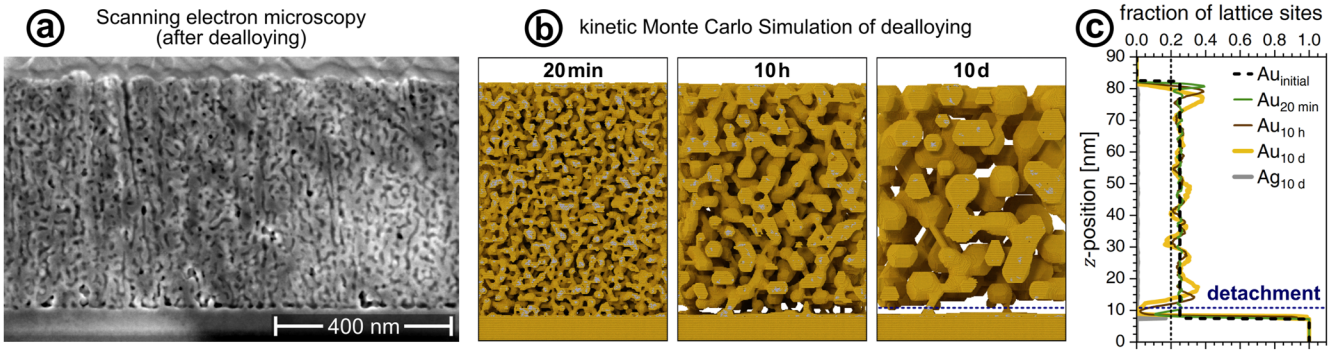

FIG. 1. Results for dealloying $Au_{25}Ag_{75}$ with uniform composition. (a) Scanning electron micrograph of an as-dealloyed film. The dark gap between the substrate and the nanoporous film indicates spontaneous loss of connectivity and material density. (b) Renderings from a kinetic Monte Carlo simulation after various dealloying durations, as indicated in the individual panels. The structure at 20 min corresponds to the end of primary dealloying. Continued evolution during secondary dealloying leads to coarsening and the emergence of a detachment layer, which becomes more pronounced over time. (c) Depth profiles of the Au density, shown as lateral averages of the Au-occupied fraction of lattice sites vs the out-of-plane coordinate z, for different time points as indicated in the legend. The dotted vertical line marks the lower density limit in the bulk region, and the dotted horizontal line indicates the z-position of maximum detachment. Note the near-zero Au density in the detachment layer after 10 days of secondary dealloying.

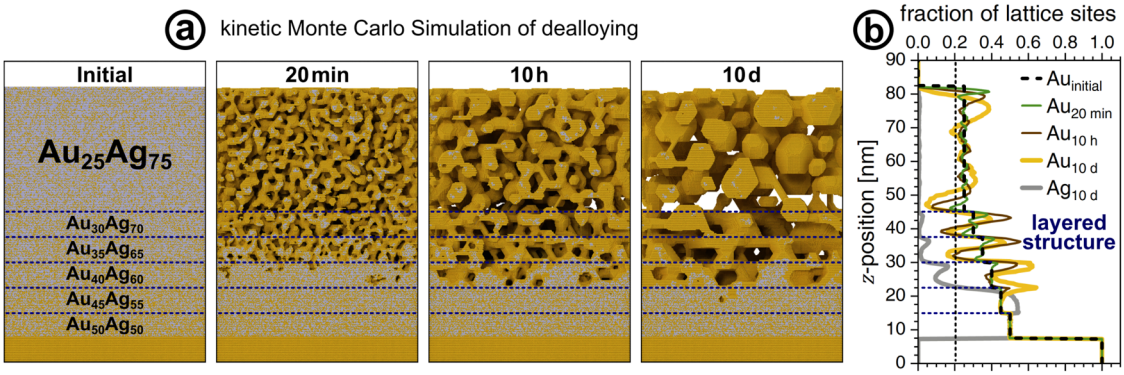

FIG. 2. Results for dealloying AuAg with a staircase composition profile. (a) Renderings from a kinetic Monte Carlo simulation after various dealloying durations, as indicated in the individual panels. The dotted blue lines mark the composition steps; uniform master alloy compositions between steps are indicated in the "initial" panel. A detachment layer emerges after 10 days at the step with the lowest Au composition and highest resulting porosity. (b) Depth profiles of the Au density, shown as lateral averages of the Au-occupied fraction of lattice sites vs the out-of-plane coordinate z, for different time points as indicated in the legend. The dotted vertical line marks the lower density limit in the bulk region, and the dotted horizontal lines indicate z-positions of the master-alloy composition steps. Systematic density reduction occurs during secondary dealloying at each step location.

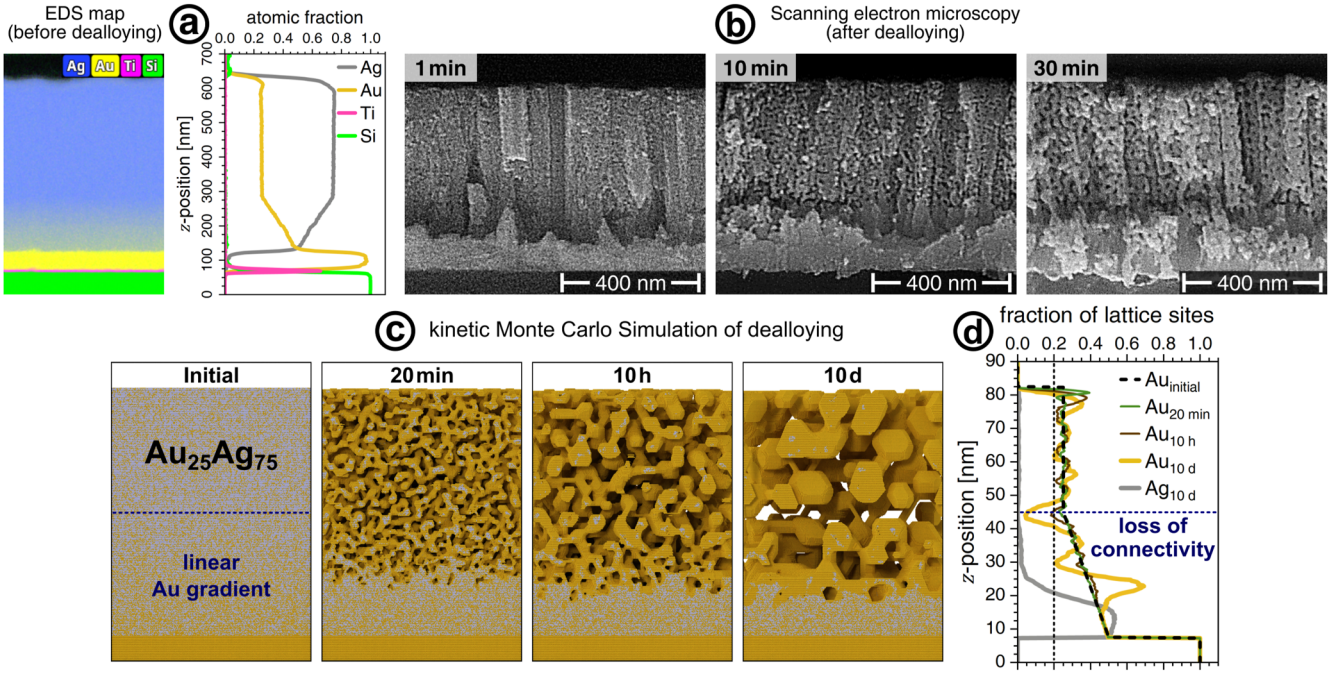

FIG. 3. Results for a composition profile with a kink. (a) Linear composition profile created by co-sputtering, shown by an elemental map from energy-dispersive x-ray spectroscopy (EDS) of a focused-ion-beam-cut lamella and the corresponding laterally averaged atom fraction profiles. The linear gradient region is bounded by the pure Au at the bottom and $Au_{25}Ag_{75}$ at the top. A distinct kink is visible at $z \approx 280$ nm. (b) Electron micrographs of electrochemically dealloyed samples based on master alloys with the composition profile in (a) and with dealloying times 1, 10, and 30 min. Data in (a) and (b) are to scale and vertically aligned. After coarsening, pronounced detachment occurs at the position of the composition kink. (c) and (d) Kinetic Monte Carlo simulation results for dealloying a system with a linear composition gradient from 50% Au at the substrate interface to 25% Au in the upper bulk region. The elements of (c) and (d) correspond to those in Figs. 1 and 2. Detachment emerges at the composition kink between the gradient and the uniform region.

after extended secondary dealloying. While the exact timeframes differ due to differences in kinetic parameters, the agreement between simulation and experiment on the film structure is strong.

Figure S5 of the supplementary material shows results similar to those of Fig. 3(b) but here for a sample dealloyed by free corrosion. The observations are quite similar, suggesting that the processes behind the decohesion act independently of the dealloying approach, free or electrochemical corrosion.

Unlike the staircase profile, the gradient one avoids abrupt composition jumps. Nevertheless, a region of reduced density with x_{Au} down to ~0.10 emerges [Fig. 3(d)], substantially lower than in the rest of the porous structure. This low-density region coincides precisely with the kink in the composition profile at the transition from gradient to uniform alloy, indicating that even smooth but non-differentiable transitions in the composition–depth (or porosity–depth) profile can trigger connectivity loss. This is not surprising in view of the link between mass flux divergences and the second derivative of the mean curvature profile, as established in Ref. 16. As will be argued below in Sec. IV, the mean curvature is expected to systematically increase with porosity, which in turn is governed by the master alloy composition. Hence, kinks in the composition profile cause discontinuities in the mean curvature profile and, consequently, flux divergences leading to loss of density and connectivity.

The findings so far demonstrate that both, discrete steps and sharp kinks, in the composition profile can trigger detachment. This implies that the optimal composition profile must be continuously differentiable to avoid abrupt changes in density or curvature. To address this, we investigated an exponential profile as a smooth and continuously differentiable alternative.

Figure 4 summarizes the results for the exponential composition profile. The simulation here studied a scenario where the Au fraction decreases exponentially from 0.50 at the substrate interface to 0.25 with a $1/e$ decay length of 18.8 nm. The corresponding experiment (top row of graphics) was here based on a master alloy with a smooth composition gradient, as shown in the EDS map of panel (a). Analysis of the laterally averaged composition–depth profile shows the gold atom fraction starting, near the substrate, at $x_{Au} = 0.50$, just above the parting limit, and decreasing to the bulk value, $x_{Au} = 0.25$, with a decay length of 85(15) nm. Starting from the substrate, the cross-sectional FIB lamella of the porous film in panel (b) (dealloyed for 30 min) shows a gradual onset of porosity and then evolution toward the uniform bulk value. Most importantly, the connectivity remains high throughout the film. The

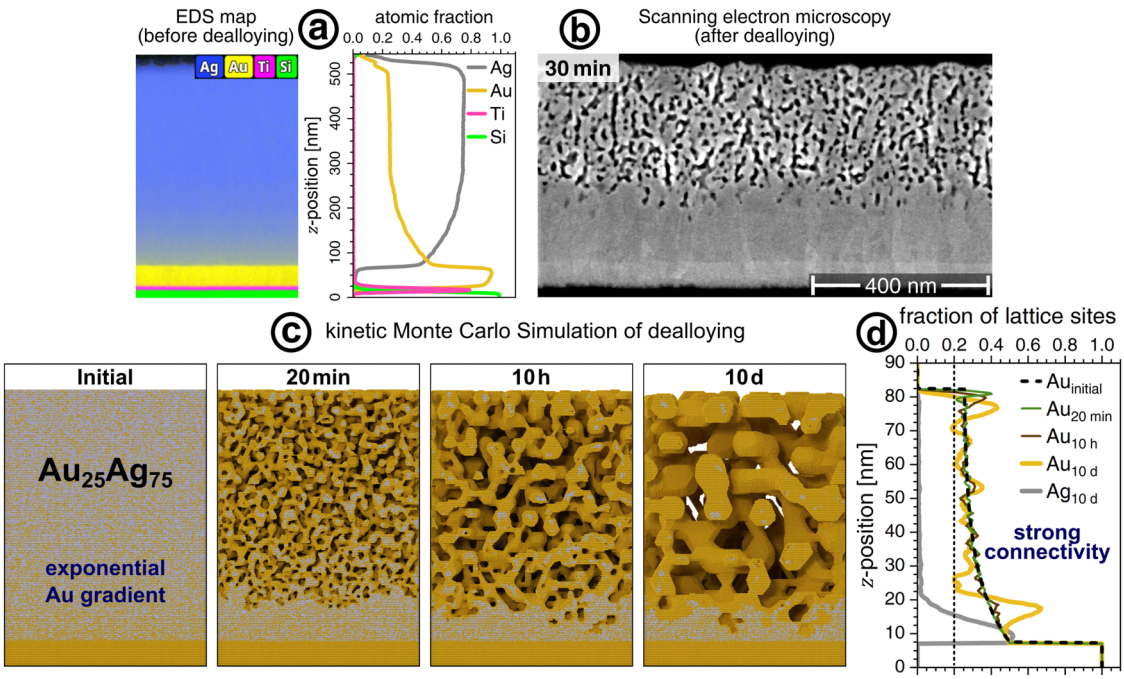

FIG. 4. Results for an exponential composition profile. The elements of this figure correspond to those in Fig. 3. (a) Exponential composition profile generated by co-sputtering, shown by an elemental map from energy-dispersive x-ray spectroscopy (EDS) of a focused-ion-beam-cut lamella and the corresponding laterally averaged atom fraction profiles. Starting from the substrate, the Au atom fraction decays smoothly from 0.50 to 0.25, with a $1/e$ decay length of 85(15) nm. Note specifically the smooth transition from gradient layer to the uniform $Au_{25}Ag_{75}$ region at the top of the film. (b) Electron micrograph of a sample with the composition profile in (a) after 30 min of electrochemical dealloying. Data in (a) and (b) are to scale and vertically aligned. The film remains cohesive throughout, with no evidence of interfacial detachment. (c) and (d) Kinetic Monte Carlo simulation results for dealloying a system with an exponential composition gradient from 50% Au at the substrate interface to 25% Au at the interface with the uniform $Au_{25}Ag_{75}$ region, with an exponential decay length of 18.8 nm. The simulated structure maintains good connectivity throughout the entire film, consistent with experimental observations.

KMC results in panels (c) and (d) are consistent with this observation. The laterally averaged solid fraction remains above 0.20 throughout the porous region, as indicated by the vertical dashed line. A minor density dip is observed around $z = 20$ nm, but it is much less pronounced than in previous profiles. Crucially, the structure remains well-connected throughout, with no indication of detachment.

Additional experiments and simulations, displayed in the supplementary material, explored steeper composition gradients in the master alloy. The experiment finds well-connected structures up to the interface, even with a decay length of 33(6) nm, which exceeds the ligament size, 10(2) nm, merely by a factor of ~3 (see Fig. S3). The extra simulation studied decay lengths down to 2.3 nm. Here, all structures are well connected after primary dealloying, and connectivity loss sets in when, upon coarsening during secondary dealloying, the mean ligament size approaches and then exceeds the decay length value (Figs. S1 and S2). These results suggest that mitigating decohesion requires the width of the porosity gradient to be larger than the final ligament size in the porous structure.

IV. DISCUSSION AND SUMMARY

In this study, we have generated substrate-supported porous films with microstructure gradients and investigated their resilience to spontaneous decohesion during the coarsening process that accompanies secondary dealloying. The gradients were achieved by tailoring the composition profile of the master alloy. As dealloying removes practically all of the less noble element while maintaining crystal lattice coherency,[33,34] the composition gradient is translated into a porosity gradient. This strategy for graded porosity was applied to the master alloys used in both kinetic Monte Carlo simulations and experiments.

Our observations confirm earlier findings, suggesting that the porous microstructure starts out well connected after primary dealloying. Moreover, the KMC data demonstrate that the initial composition profile is replicated into a porosity profile of similar functional form during primary dealloying. However, coarsening during the subsequent secondary dealloying can redistribute matter so as to generate regions of exceptionally low density. This process can lead to a pronounced loss of connectivity in specific layers parallel to the interface. These low-density, low-connectivity regions compromise the adhesion to the substrate or the internal cohesion of the films. Surface-diffusion-mediated coarsening is an intrinsic process in porous materials. At the same time, the film–substrate interface inherently presents a microstructural heterogeneity. As a result, spontaneous decohesion may be a generic feature of such systems, not limited to dealloyed structures.

Simulations and experiments consistently link the connectivity loss to discontinuities in either the density–depth profile itself or its first derivative. This aligns with the discussion in Ref. 16, which identifies the second derivative of the laterally averaged surface curvature as a source of mass flux divergence. According to the transport continuity equation, such flux divergence leads to local accumulation or depletion of material and thus to evolving porosity.

It is not firmly established how the mean curvature of dealloyed porous structures, such as those of the present study, depends on the master alloy composition at any given constant value of the dealloying potential. Assuming that the characteristic microstructure length scale remains sensibly constant, the increased porosity that comes with an increased less-noble element fraction entails slimmer ligaments and, hence, an increased surface mean curvature. This would tie the mean curvature to the master alloy composition, in keeping with the present observations.

At the interface between the porous film and its massive substrate, pores must terminate, requiring concave surfaces with more negative curvature than typical ligament surfaces. Consequently, a gradient in the surface mean curvature is an inherent attribute of the interface. The segments of concave surface act as preferential sinks for atoms migrating by surface diffusion, which depletes adjacent ligaments of material, a process that may terminate in ligament pinch off and, hence, decohesion. Thus, it may not be possible to completely avoid density loss during coarsening. Our study shows that good cohesion can still be maintained, provided that the initial porosity gradient is designed so as to have a low porosity at the interface. This exploits that less porous (higher density) microstructures are more resilient to loss of connectivity, as it is represented by the scaled topological genus.[21]

It is well established that thin films on substrates generally exhibit growth stress[35] and that this stress—be it tensile or compressive—may impair adhesion or promote delamination in the form of stress-driven crack propagation along the film–substrate interface.[36] When a substrate-supported film is dealloyed, the trend for dealloying-induced shrinkage of the stress-free alloy[33,37] along with the in-plane clamping constraints may induce substantial tensile stress,[38] and this may result in through-film cracks.[39] Protocols have been established for mitigating shrinkage[33,37] and stress in the dealloyed films.[40,41] Remarkably, even when the film stress remains below the value that induces through-film cracking, a loss of interfacial cohesion may still be observed [Fig. 8(c) in Ref. 40]. This underlines the distinction between decohesion and crack formation. Decohesion, as studied in the present work, takes the form of the pinch-off of ligaments or, more generally, of solid bridges by diffusion that is driven by capillarity rather than stress. The agreement between our experimental observations and our simulation on a rigid—hence, stress-free—lattice confirms that stress is here not the primary driving force for decohesion.

In our study, porosity was generated by dealloying Ag–Au and the porosity gradients resulted from gradients in the master alloy composition and the approach of that composition to the parting limit, that is, to the minimum content of the less-noble component required for through-bulk dealloying.[30] As the parting limit is to some degree alloy-specific, different master alloys will require different composition profiles. In sintered porous interconnects, porosity gradients might be generated through gradients in particle size or in slurry solid fraction.

By comparing the microstructure evolution during secondary dealloying and coarsening of graded porous microstructures, this study has unraveled criteria for material design mitigating the loss of cohesion at the interface between porous structures and massive substrates. We have pointed out that the underlying mechanisms act quite generally at such interfaces, whenever curvature-driven mass transport is active. Since curvature driven diffusion is fundamentally the mechanism behind sintering, we expect that these considerations apply quite widely to the processing of porous materials.

Our study identifies two key design principles to improve cohesion in porous materials: (1) employing smooth, continuously differentiable porosity profiles to minimize curvature-driven diffusion and (2) confining steep porosity gradients to regions with initially low porosity, thereby preserving microstructural connectivity. The gradient layer requires a minimum thickness in the order of the ligament size. When function requires a given thickness of the open porous material, then the total porous film thickness needs to be increased accordingly. The insights gained here are relevant for optimizing the stability of dealloyed catalysts, porous electrodes, and sintered metallic interconnects, with particular relevance for microelectronics and energy conversion technologies.

SUPPLEMENTARY MATERIAL

See the supplementary material for the following:

- An account (descriptive text and Figs. S1–S3) of additional simulations and experiments probing master alloys with exponential composition gradients of different decay lengths. This account also includes (as Fig. S4) wider field-of-view versions of the electron micrographs for the linear-gradient sample in Fig. 3. Furthermore, it shows experimental data on a film dealloyed by free corrosion (Fig. S5).
- Four video files illustrating the microstructure evolution in the kinetic Monte Carlo simulation, one file for each of the four separate dealloying simulations underlying Figs. 1–4. Each video shows simulation renderings based on frames recorded after exponentially increasing time intervals.

ACKNOWLEDGMENTS

Funding by Deutsche Forschungsgemeinschaft through Grant No. WE 1424/19-1 and assistance by Tobias Krekeler, Dagmar Rings, and Gunnar Schaan from Hamburg University of Technology's Electron Microscopy Unit are gratefully acknowledged.

AUTHOR DECLARATIONS

Conflict of Interest

The authors have no conflicts to disclose.

Author Contributions

Gideon Henkelmann: Conceptualization (equal); Investigation (lead); Validation (equal); Writing – original draft (equal); Writing – review & editing (equal). **Xinyan Wu**: Investigation (equal); Validation (equal); Writing – original draft (supporting); Writing – review & editing (supporting). **Jörg Weissmüller**: Conceptualization (supporting); Funding acquisition (lead); Investigation (equal); Supervision (lead); Writing – original draft (equal); Writing – review & editing (equal).

DATA AVAILABILITY

The data that support the findings of this study are available from the corresponding author upon reasonable request.

REFERENCES

[1]M. C. Dixon, T. A. Daniel, M. Hieda, D. M. Smilgies, M. H. W. Chan, and D. L. Allara, "Preparation, structure, and optical properties of nanoporous gold thin films," Langmuir **23**, 2414–2422 (2007).
[2]M. M. P. Arnob, F. Zhao, J. Li, and W.-C. Shih, "EBL-based fabrication and different modeling approaches for nanoporous gold nanodisks," ACS Photonics **4**, 1870–1878 (2017).
[3]O. Kurtulus, P. Daggumati, and E. Seker, "Molecular release from patterned nanoporous gold thin films," Nanoscale **6**, 7062–7071 (2014).
[4]M. Graf, D. Jalas, J. Weissmüller, A. Y. Petrov, and M. Eich, "Surface-to-volume ratio drives photoelelectron injection from nanoscale gold into electrolyte," ACS Catal. **9**, 3366–3374 (2019).
[5]H.-J. Qiu, H.-T. Xu, L. Liu, and Y. Wang, "Correlation of the structure and applications of dealloyed nanoporous metals in catalysis and energy conversion/storage," Nanoscale **7**, 386–400 (2015).
[6]Z. Zeng, X. Long, H. Zhou, E. Guo, X. Wang, and Z. Hu, "On-chip interdigitated supercapacitor based on nano-porous gold/manganese oxide nanowires hybrid electrode," Electrochim. Acta **163**, 107–115 (2015).
[7]Q. Chen, Y. Ding, and M. Chen, "Nanoporous metal by dealloying for electrochemical energy conversion and storage," MRS Bull. **43**, 43–48 (2018).
[8]K.-U. Lee, J. Y. Byun, H.-J. Shin, and S. H. Kim, "A high-performance supercapacitor based on polyaniline-nanoporous gold," J. Alloys Compd. **779**, 74–80 (2019).
[9]N. V. Lavrik, C. A. Tipple, M. J. Sepaniak, and P. G. Datskos, "Gold nanostructures for transduction of biomolecular interactions into micrometer scale movements," Biomed. Microdevices **3**, 35–44 (2001).
[10]D. Kramer, R. N. Viswanath, and J. Weissmüller, "Surface-stress induced macroscopic bending of nanoporous gold cantilevers," Nano Lett. **4**, 793–796 (2004).
[11]E. Seker, M. L. Reed, and M. R. Begley, "Nanoporous gold: Fabrication, characterization, and applications," Materials **2**, 2188–2215 (2009).
[12]X. Li, M. Liu, B. Huang, H. Liu, W. Hu, L.-H. Shao, and Z. L. Wang, "Nanoporous-gold-based hybrid cantilevered actuator dealloyed and driven by a modified rotary triboelectric nanogenerator," Sci. Rep. **6**, 24092 (2016).
[13]A. Chauvin, N. Stephant, K. Du, J. Ding, I. Wathuthanthri, C.-H. Choi, P.-Y. Tessier, and A.-A. El Mel, "Large-scale fabrication of porous gold nanowires via laser interference lithography and dealloying of gold–silver nano-alloys," Micromachines **8**, 168 (2017).
[14]K. Mohan, N. Shahane, R. Liu, V. Smet, and A. Antoniou, "A review of nanoporous metals in interconnects," JOM **70**, 2192–2204 (2018).
[15]L. Dietrich, H. Oppermann, C. Lopper, and P. Mackowiak, "Fabrication and characterization of nanoporous gold (NPG) interconnects for wafer level packaging," in *2022 IEEE 72nd Electronic Components and Technology Conference (ECTC)* (IEEE, 2022), pp. 873–882.
[16]G. Henkelmann, D. Waldow, M. Liu, L. Lührs, Y. Li, and J. Weissmüller, "Self-detachment and subsurface densification of dealloyed nanoporous thin films," Nano Lett. **22**, 6787–6793 (2022).
[17]C. M. Müller and R. Spolenak, "Microstructure evolution during dewetting in thin Au films," Acta Mater. **58**(18), 6035–6045 (2010).
[18]A. Kosinova, O. Kovalenko, L. Klinger, and E. Rabkin, "Mechanisms of solid-state dewetting of thin Au films in different annealing atmospheres," Acta Mater. **83**, 91–101 (2015).
[19]F. Leroy, Ł. Borowik, F. Cheynis, Y. Almadori, S. Curiotto, M. Trautmann, J. C. Barbé, and P. Müller, "How to control solid state dewetting: A short review," Surf. Sci. Rep. **71**(2), 391–409 (2016).
[20]F. Yu, R. W. Johnson, and M. C. Hamilton, "Pressureless sintering of microscale silver paste for 300 °C applications," IEEE Trans. Compon., Packag., Manuf. Technol. **5**, 1258–1264 (2015).

[21] Y. Li, B.-N. Dinh Ngô, J. Markmann, and J. Weissmüller, "Topology evolution during coarsening of nanoscale metal network structures," Phys. Rev. Mater. **3**, 076001 (2019).
[22] J. C. M. Hwang, J. D. Pan, and R. W. Balluffi, "Measurement of grain-boundary diffusion at low temperature by the surface-accumulation method. II. Results for gold-silver system," J. Appl. Phys. **50**(3), 1349–1359 (1979).
[23] J. D. Pan and R. W. Balluffi, "Diffusion induced grain boundary migration in and thin films," Acta Metall. **30**(4), 861–870 (1982).
[24] A. Bukaluk, "Analysis of diffusion mechanisms in thin polycrystalline Au–Ag films using auger electron spectroscopy," Surf. Interface Anal. **5**(1), 20–27 (1983).
[25] N. Gazit, L. Klinger, G. Richter, and E. Rabkin, "Formation of hollow gold-silver nanoparticles through the surface diffusion induced bulk intermixing," Acta Mater. **117**, 188–196 (2016).
[26] J. Erlebacher, "An atomistic description of dealloying," J. Electrochem. Soc. **151**, C614 (2004).
[27] J. Erlebacher, "Mechanism of coarsening and bubble formation in high-genus nanoporous metals," Phys. Rev. Lett. **106**, 225504 (2011).
[28] T. Krekeler, A. V. Straßer, M. Graf, K. Wang, C. Hartig, M. Ritter, and J. Weissmüller, "Silver-rich clusters in nanoporous gold," Mater. Res. Lett. **5**, 314–321 (2017).
[29] Y. Li, B.-N. Ngo-Dinh, J. Markmann, and J. Weissmüller, "Evolution of length scales and of chemical heterogeneity during primary and secondary dealloying," Acta Mater. **222**, 117424 (2022).
[30] D. M. Artymowicz, J. Erlebacher, and R. C. Newman, "Relationship between the parting limit for de-alloying and a particular geometric high-density site percolation threshold," Philos. Mag. **89**, 1663–1693 (2009).
[31] A. Stukowski, "Visualization and analysis of atomistic simulation data with OVITO–the open visualization tool," Modell. Simul. Mater. Sci. Eng. **18**, 015012 (2009).
[32] M. Andersen, C. Panosetti, and K. Reuter, "A practical guide to surface kinetic Monte Carlo simulations," Front. Chem. **7**, 202 (2019).
[33] S. Parida, D. Kramer, C. A. Volkert, H. Rösner, J. Erlebacher, and J. Weissmüller, "Volume change during the formation of nanoporous gold by dealloying," Phys. Rev. Lett. **97**(3), 035504 (2006).
[34] H. J. Jin, L. Kurmanaeva, J. Schmauch, H. Rösner, Y. Ivanisenko, and J. Weissmüller, "Deforming nanoporous metal: Role of lattice coherency," Acta Mater. **57**(9), 2665–2672 (2009).
[35] G. Abadias, E. Chason, J. Keckes, M. Sebastiani, G. B. Thompson, E. Barthel, G. L. Doll, C. E. Murray, C. H. Stoessel, and L. Martinu, "Review article: Stress in thin films and coatings: Current status, challenges, and prospects," J. Vac. Sci. Technol., A **36**(2), 020801 (2018).
[36] D. B. Marshall and A. G. Evans, "Measurement of adherence of residually stressed thin films by indentation. I. Mechanics of interface delamination," J. Appl. Phys. **56**(10), 2632–2638 (1984).
[37] X.-L. Ye, N. Lu, X.-J. Li, K. Du, J. Tan, and H.-J. Jin, "Primary and secondary dealloying of Au(Pt)-Ag: Structural and compositional evolutions, and volume shrinkage," J. Electrochem. Soc. **161**(12), C517–C526 (2014).
[38] Y. Sun, K. P. Kucera, S. A. Burger, and T. John Balk, "Microstructure, stability and thermomechanical behavior of crack-free thin films of nanoporous gold," Scr. Mater. **58**(11), 1018–1021 (2008).
[39] X. Lu, T. J. Balk, R. Spolenak, and E. Arzt, "Dealloying of Au–Ag thin films with a composition gradient: Influence on morphology of nanoporous Au," Thin Solid Films **515**(18), 7122–7126 (2007).
[40] O. Okman and J. W. Kysar, "Fabrication of crack-free blanket nanoporous gold thin films by galvanostatic dealloying," J. Alloys Compd. **509**(22), 6374–6381 (2011).
[41] E. Seker, J. T. Gaskins, H. Bart-Smith, J. Zhu, M. L. Reed, G. Zangari, R. Kelly, and M. R. Begley, "The effects of annealing prior to dealloying on the mechanical properties of nanoporous gold microbeams," Acta Mater. **56**(3), 324–332 (2008).